

Consistency between real and synthetic fast-ion measurements at ASDEX Upgrade

J Rasmussen¹, S K Nielsen¹, M Stejner¹, B Geiger²,
M Salewski¹, A S Jacobsen¹, S B Korsholm¹, F Leipold¹,
P K Michelsen¹, D Moseev^{2,3}, M Schubert², J Stober²,
G Tardini², D Wagner², and the ASDEX Upgrade Team²

¹ Technical University of Denmark, Department of Physics, Fysikvej, building 309, DK-2800 Kgs. Lyngby, Denmark

² Max-Planck-Institut für Plasmaphysik, Boltzmannstr. 2, D-85748 Garching, Germany

³ FOM Institute DIFFER, 3430 BE Nieuwegein, The Netherlands

E-mail: jeras@fysik.dtu.dk

Abstract. Internally consistent characterization of the properties of the fast-ion distribution from multiple diagnostics is a prerequisite for obtaining a full understanding of fast-ion behavior in tokamak plasmas. Here we benchmark several absolutely-calibrated core fast-ion diagnostics at ASDEX Upgrade by comparing fast-ion measurements from collective Thomson scattering, fast-ion D_α spectroscopy, and neutron rate detectors with numerical predictions from the TRANSP/NUBEAM transport code. We also study the sensitivity of the theoretical predictions to uncertainties in the plasma kinetic profiles. We find that theory and measurements generally agree within these uncertainties for all three diagnostics during heating phases with either one or two neutral beam injection sources. This suggests that the measurements can be described by the same model assuming classical slowing down of fast ions. Since the three diagnostics in the adopted configurations probe partially overlapping regions in fast-ion velocity space, this is also consistent with good internal agreement among the measurements themselves. Hence, our results support the feasibility of combining multiple diagnostics at ASDEX Upgrade to reconstruct the fast-ion distribution function in 2D velocity space.

PACS numbers: 52.25.Os, 52.40.Db, 52.50.Gj, 52.65.Cc, 52.70.Gw

1. Introduction

Fast ions with supra-thermal velocities play a key role in heating the plasma in current and future fusion devices. In particular, fast fusion-born alpha particles in next-step burning fusion devices must be well confined, both to maintain fusion-relevant temperatures through transfer of their kinetic energy to the background plasma, and to reduce their otherwise deleterious impact on the plasma-facing components. Fast ions can furthermore both drive and interact with a range of common plasma

instabilities [1–8] and may thus have an important impact on the overall stability and performance of the plasma. Accurate characterization and detailed understanding of the behaviour of fast-ion populations in tokamak plasmas are thus important for attempts to optimize plasma heating, current drive, and overall fusion performance, and ultimately to achieve stable burning conditions in a future fusion power plant. At the medium-sized (major plasma radius $R = 1.65$ m) ASDEX Upgrade (AUG) tokamak, a wide range of diagnostics exist for this purpose, including fast-ion D_α spectroscopy (FIDA) [5, 9–11], collective Thomson scattering (CTS) [12–16], fast-ion loss detectors [17], neutral particle analyzers [18], neutron rate detectors [19, 20], and neutron [21, 22] and γ -ray spectrometers [23]. Combined with the flexible and powerful auxiliary heating systems [24], this extensive suite of instruments makes AUG particularly well equipped for fast-ion studies among current fusion experiments.

Each of the fast-ion diagnostics at AUG has a specific viewing geometry. By combining multiple views from one or more diagnostics it is, in principle, possible to obtain a 2D velocity-space reconstruction of the fast-ion velocity distribution function [25–28]. A prerequisite for obtaining sensible results from this technique is that fast-ion measurements from the involved diagnostics be broadly mutually consistent. However, testing for consistency among different diagnostics is non-trivial, as each diagnostic has a different sensitivity to ions associated with specific regions in real space and velocity space (e.g. [29]). In particular, the real-space and velocity-space regions accessible by different diagnostics may not even overlap, resulting in each diagnostic sampling separate sub-populations of fast ions.

As a first step in addressing this problem, one can compare experimental results from different diagnostics to theoretical predictions based on the same set of assumptions. In this work, we compare synthetic and real measurements from three absolutely-calibrated diagnostics at AUG that are sensitive to the fast-ion distribution function in the plasma core: CTS, FIDA, and neutron rate detectors. CTS at AUG can measure a 1D projection of the fast-ion velocity distribution and is based on launching a millimeter-wave probe beam into the plasma and collecting part of the resulting radiation that is scattered off mainly ion-driven microscopic plasma fluctuations. The FIDA diagnostic can measure spectra of Doppler-shifted Balmer- α ($n = 3 \rightarrow 2$) radiation at several spatial locations. The FIDA light arises due to fast deuterium ions which become neutralized through charge exchange reactions with neutral beam injected particles. Both CTS and FIDA represent localized measurements, with the signal arising in relatively small measurement volumes. If multiple CTS or FIDA geometries probing the same position are available, the 2D fast-ion velocity distribution can be reconstructed [25–28]. In addition, we also consider the neutron rate (i.e., the volume-integrated neutron flux), which is a measure of the rate of fusion reactions in the plasma and so is sensitive to the energy and density of fast ions. In contrast to CTS and FIDA, the neutron rate detectors at AUG are sensitive to the full plasma volume, although the neutron production is generally dominated by reactions in the plasma core.

Here we present and benchmark results obtained from these three diagnostics for

the fast-ion populations in AUG discharge 29600. In section 2, we provide an overview of the discharge and of the measurements and data analysis pertaining to each diagnostic. Some emphasis is placed on the analysis of CTS spectra obtained in this discharge, as this has been described only in limited detail elsewhere [16, 30]. In section 3, we present and contrast the results from each diagnostic with predictions based on the TRANSP/NUBEAM code, and section 4 compares and discusses these findings. We close with a summary and outlook in section 5.

2. Measurements and analysis

The measured and synthetic data presented in this work are based on measurements obtained in AUG discharge 29600. This was a standard H-mode discharge with a D plasma, a toroidal field $B_t = -2.56$ T, plasma current $I_p = 0.8$ MA, and core electron density $n_e \approx 6.0 \times 10^{19} \text{ m}^{-3}$. Co-current neutral beam injection (NBI) from two sources with similar injection geometries and on-axis deposition profiles, Q3 (60 keV injection energy for D) and Q8 (93 keV), was employed both independently and together during the discharge to allow studies of the slowing down of fast ions in the plasma. Figure 1 presents an overview of the discharge. In terms of magnetohydrodynamic (MHD) activity, the plasma was fairly quiescent, the most prominent activity being a (2,1) neo-classical tearing mode (NTM) triggered at $t = 5.73$ s following the termination of the two-beam NBI phase. In addition, soft X-ray data suggest the presence of modest sawtooth activity from $t = 3.5$ – 4.2 s, with much smaller sawteeth later in the discharge.

Among the fast-ion diagnostics considered here, neutron rates were monitored throughout the discharge. CTS data were acquired during all heating phases, but with a duration limited by machine requirements associated with the amount of energy deposited by unabsorbed microwave probe radiation. FIDA data, being based on charge exchange reactions with neutrals injected by NBI Q3, were obtained during all Q3 phases.

2.1. CTS

The CTS system at AUG employs a gyrotron which generates mm-wave probing radiation at $f_{\text{gyr}} \simeq 105$ GHz [12, 14–16, 31]. The CTS signal is absolutely calibrated using two blackbody sources at different temperatures [31]. The measurements discussed here employed the new dual-receiver background technique described in [16], with a passive-view receiver system whose field of view does not intersect the probing beam. This enables accurate background characterization, which is particularly important for fast-ion measurements where the CTS spectral power densities are relatively low. We note from Figure 1(e) that the background-subtracted CTS signal is indeed negligible at large frequency shifts during phases with no NBI heating (and hence with no supra-thermal ions in the plasma). Further proof-of-principle measurements and first applications of the new CTS dual-receiver technique can be found in [16, 30], while the acquisition,

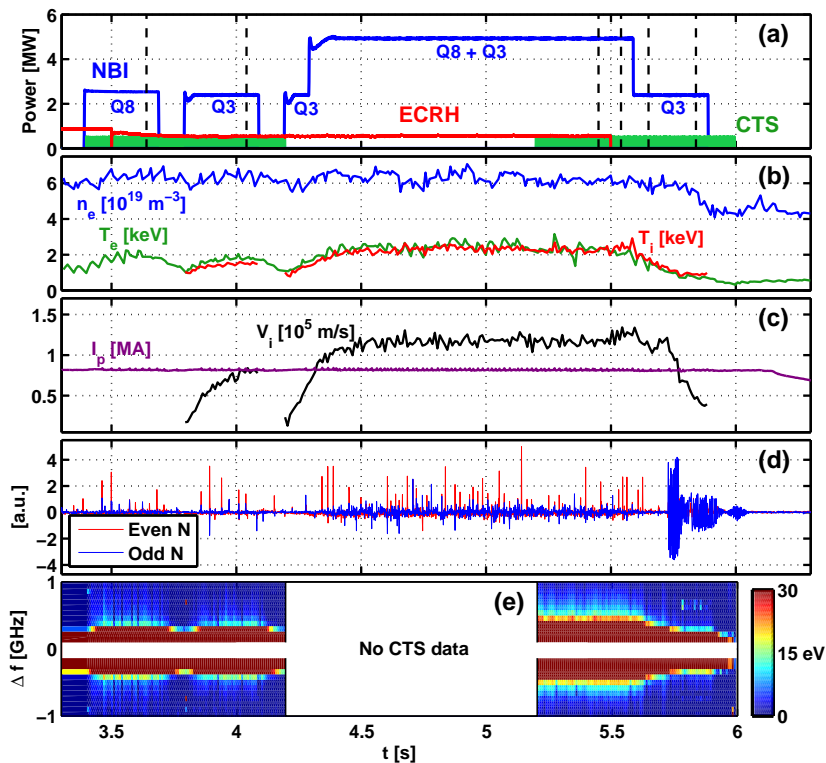


Figure 1. Overview of AUG discharge 29600. (a) Time traces of injected NBI, central 140 GHz electron cyclotron resonance heating (ECRH), and 105 GHz CTS probe power. Dashed vertical lines indicate the times where we compare the measurements with TRANSP (section 2.4). (b) Core electron density and temperature from incoherent Thomson scattering and ion temperature from charge exchange recombination spectroscopy (CXRS) on boron, all mapped to the CTS measurement volume. (c) Toroidal plasma rotation velocity from CXRS (mapped to the CTS volume) and plasma current. (d) MHD activity (even and odd toroidal mode numbers) as measured by magnetic field coils. A (2,1) NTM is present from $t = 5.73$ s. (e) CTS spectrogram centered on the probe gyrotron frequency, showing spectral power densities outside the stopbands of the central notch filters.

calibration, and background subtraction of time-resolved CTS spectra are described in detail in [16, 31].

For discharge 29600, the scattering volume defined by the intersection of the probe beam and the receiver view was placed near the center of the plasma at $(R, z) = (1.73, -0.11)$ m, corresponding to a normalized poloidal flux coordinate of $\rho_{\text{pol}} \simeq 0.36$ as calculated from raytracing. The CTS temporal and radial resolution for this discharge were 6–8 ms and 6 cm, respectively. The angle between the wave vector $\mathbf{k}^\delta = \mathbf{k}^s - \mathbf{k}^i$ of the resolved plasma fluctuations and the magnetic field vector was $\phi = \angle(\mathbf{k}^\delta, \mathbf{B}) = 106^\circ$, where \mathbf{k}^i and \mathbf{k}^s are the wave vectors of the incident and scattered (received) radiation, respectively. The resulting scattering angle was $\theta = \angle(\mathbf{k}^i, \mathbf{k}^s) = 122^\circ$. Figure 2 illustrates the scattering geometry and the paths of the probing beam, the active receiver view, and the passive view for background

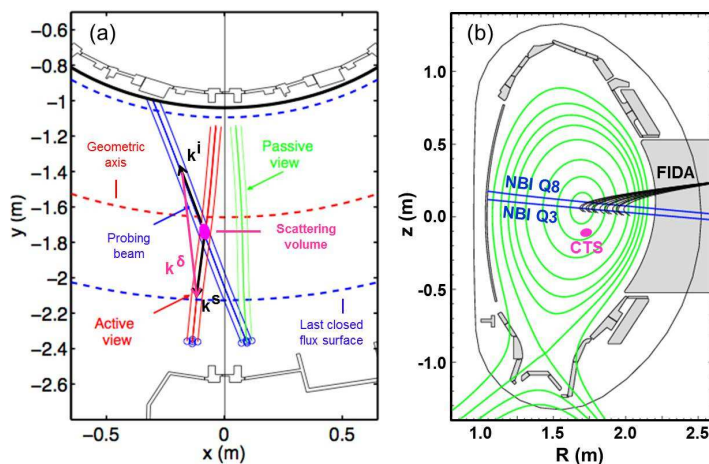


Figure 2. (a) CTS geometry in a toroidal view for ASDEX Upgrade discharge 29600. The gyrotron probe beam (blue) overlaps with the receiver view (red) in the scattering volume (magenta). For this viewing geometry, the resolved fluctuation vector \mathbf{k}^δ makes an angle of 106° to the magnetic field. (b) Location of the CTS volume (magenta) in a poloidal view, along with the 13 toroidal FIDA lines of sight used here (black). Also shown are the paths of the NBI Q3 and Q8 beams (blue), and magnetic flux surfaces (green) at normalized poloidal flux $\rho_{\text{pol}} = 0.2, 0.4, 0.6, 0.8, 0.9, 0.95, 1.0, \text{ and } 1.05$.

measurements.

The CTS spectral analysis presented here employs a forward model of the scattering [32,33], which includes contributions from (neutral beam generated) fast D ions, thermal D and H ions, and thermal electrons and impurity species in the background plasma – here ^4He , ^{12}C , ^{56}Fe , and ^{183}W . In order to calculate synthetic CTS spectra, this model is combined with the fast-ion velocity distribution in the scattering volume predicted by the TRANSP transport code coupled with the neutral beam module NUBEAM [34]. The resulting synthetic spectra are compared to experimental CTS spectra extracted as in [16]. To allow a similar comparison in fast-ion velocity space, the 1D (fast) ion velocity distribution $g(u)$,

$$g(u) = \int f(\mathbf{v}) \delta\left(\frac{\mathbf{v} \cdot \mathbf{k}^\delta}{k^\delta} - u\right) d\mathbf{v}, \quad (1)$$

i.e., the projection of the fast-ion distribution function onto \mathbf{k}^δ , is inferred by fitting the measured CTS spectra with the above scattering model. Here $\delta(\dots)$ is the Dirac δ -function and u is the projected velocity along \mathbf{k}^δ . The result is then compared with that predicted by TRANSP. Further details of this procedure can be found in, e.g., [14].

The spectral fitting is performed within a Bayesian framework, taking priors for fit parameters and their uncertainties as determined from other diagnostics whenever possible [35]. Table 1 summarizes the fit parameters and their values or sources of their priors. A number of well-determined, discharge- or CTS-specific parameters are kept fixed in the fit in order to reduce the number of free parameters, although their uncertainties are still taken into account in the Bayesian inference. These parameters

include the location (R, z) of the scattering volume and the scattering geometry defined by θ , ϕ , and the azimuthal angle $\psi = \angle(\mathbf{k}^i \times \mathbf{B}, \mathbf{k}^s \times \mathbf{B})$. These are all estimated from raytracing, with uncertainties based on their temporal variations. The overlap O_b , which describes the gyrotron beam width at the scattering location and its spatial overlap with the receiver beam, is determined [36] from

$$O_b = \frac{\exp[-2D^2/(W_i^2 + W_s^2)]}{|\sin \theta| \sqrt{\frac{\pi}{2}(W_i^2 + W_s^2)}}. \quad (2)$$

Here the Gaussian half-widths $W_i \simeq W_s \simeq 0.03$ m of the probe and receiver beams, respectively, are obtained from our in-vessel measurements, and the distance D between the beam centers is assumed to be zero. In addition to these parameters, we also fix the magnitude B of the magnetic field in the CTS volume at the value obtained from equilibrium reconstruction, and the electron temperature and density are maintained at the values obtained from Integrated Data Analysis (IDA [37]). Finally, a fast digitizer provides high frequency resolution measurements of the thermal (bulk ion) CTS spectrum [31]. This is used to accurately determine the probing gyrotron frequency f_{gyr} , which is also fixed in the fit as is the injected gyrotron power P_i .

The remaining, free, fit parameters include the ion temperature and toroidal rotation velocity, with fit priors taken from CXRS measurements (interpolated to ρ_{pol} of the CTS volume) when available, and otherwise from our fits to the CTS bulk-ion fast digitizer data [38]. We also fit the isotope ratio $R_i = n_H/(n_D + n_H)$ involving the hydrogen and deuterium densities n_H and n_D , respectively, taking $R_i = 0.02$ as prior. All impurity concentrations (using priors from CXRS and grazing incidence X-ray spectroscopy for n_{He} and n_W , respectively) are furthermore allowed to vary, as is the overall scaling of the spectrum in order to allow for uncertainties in the probe/receiver beam overlap, the gyrotron power, and the absolute calibration. Each fit thus involves eight free parameters – in addition to those describing $g(u)$ – many of which are already well constrained from other diagnostics. The values of the fit parameters or the sources of their priors, as summarized in table 1, are also adopted for the calculation of synthetic CTS spectra. Uncertainties on all fit results include those arising from temporal variations in the CTS data.

2.2. FIDA

Each of the FIDA views installed at AUG samples a distinct region in real space and fast-ion velocity space and consists of multiple lines of sight, allowing spatially resolved measurements. For discharge 29600, data were available from one of the toroidal FIDA views, with an angle of $\phi \approx 12^\circ$ to the magnetic field. Along this view, 13 lines of sight were connected to the FIDA spectrometer during the discharge as illustrated in figure 2. Combining data from these separate sight lines permits the construction of a radial FIDA intensity profile, with a typical radial resolution of ± 3 cm [9].

The analysis of FIDA spectra for the discharge followed the approach outlined in [5], with further details of the FIDA diagnostic at AUG and its absolute calibration

Table 1. Fixed and free parameters in the CTS scattering model.

Parameter	Symbol	Value or prior
Fixed:		
Electron temperature	T_e	Value from IDA
Electron density	n_e	From IDA
Magnitude of magnetic field	B	2.47 ± 0.05 T
Injected gyrotron power	P_i	450 ± 50 kW
Gyrotron frequency	f_{gyr}	104.92 GHz
Scattering location	(R, z)	$(1.73, -0.11) \pm 0.01$ m
Projection angle, $\angle(\mathbf{k}^\delta, \mathbf{B})$	ϕ	$106 \pm 1^\circ$
Scattering angle, $\angle(\mathbf{k}^i, \mathbf{k}^s)$	θ	$122 \pm 1^\circ$
Azimuthal angle, $\angle(\mathbf{k}^i \times \mathbf{B}, \mathbf{k}^s \times \mathbf{B})$	ψ	$156 \pm 1^\circ$
Beam overlap	O_b	22 ± 2 m ⁻¹
Fitted:		
Ion temperature	T_i	From CXRS (or CTS)
Ion rotation velocity	V_i	From CXRS (or CTS)
Isotope ratio $n_H/(n_H + n_D)$	R_i	0.02 ± 0.02
He impurity concentration	n_{He}/n_e	0.03 ± 0.01 (from CXRS)
C impurity concentration	n_{C}/n_e	0.001 ± 0.001
Fe impurity concentration	n_{Fe}/n_e	0.001 ± 0.001
W impurity concentration	n_{W}/n_e	From X-ray spectroscopy

provided in [9]. The bremsstrahlung background present in the spectra was subtracted assuming a constant, uniform contribution across the relevant wavelength range. Passive FIDA radiation, which originates from fast ions undergoing charge exchange with edge neutrals, can contribute significantly to the measured spectra during off-axis NBI heating [9]. This contribution can be monitored when NBI Q3 is off, and it is negligible, of order 5%, in the present discharge, which only involves on-axis heating. It has consequently not been subtracted from the measured spectra, as it has no significant bearing on any of our results. The total FIDA light originating from a given volume scales with the product of local fast-ion and neutral densities [29], of which the latter can be estimated from the beam emission component in the spectra. This component represents D_α radiation from NBI particles which are excited by collisions with the target plasma. Hence, the observed FIDA radiation was normalized by the beam emission to provide an experimentally accessible proxy for the fast-ion density in the measurement volume.

2.3. Neutron rates

As a complement to CTS and FIDA, we also consider the neutron rates generated in the plasma. In NBI-heated discharges at AUG (which include most H-mode plasmas), neutron production takes place primarily in D-D reactions between NBI particles and the target plasma, so the measured neutron rates reflect the underlying distribution function of supra-thermal ions. Here we use the corrected supra-thermal neutron rates from the

five neutron rate detectors installed at AUG [19, 20]. These detectors are co-located outside the torus, with descending sensitivities that allow them to cover a large dynamic range ($\sim 10^9$ – 10^{16} neutrons/s) with a typical time resolution of 1 ms. The detectors are mounted inside a polyethylene barrel which thermalizes incoming neutrons to make the detection efficiency independent of the initial neutron energy. Like the CTS and FIDA diagnostics, the highest-sensitivity neutron detectors are absolutely calibrated (using an in-vessel PuBe source). This calibration is transferred to the other detectors using the neutron rates measured in plasma discharges. However, unlike CTS and FIDA (and the more recently installed neutron spectrometer [21]), the neutron rate detectors have no directional sensitivity and hence do not perform spatially resolved measurements, as they simply count the total neutron production coming from all directions.

2.4. TRANSP/NUBEAM simulations

In order to compare the results from each diagnostic to theoretical predictions, we ran TRANSP/NUBEAM simulations to obtain the expected fast-ion distribution function and neutron rates, given the inferred plasma equilibrium and plasma and NBI parameters. These simulations assumed neo-classical fast-ion transport, electron kinetic profiles obtained from IDA based on Thomson scattering and deuterium cyanide (DCN) laser interferometry, ion temperatures and toroidal rotation velocities from CXRS, and a spatially constant (but time-varying) effective charge Z_{eff} derived from bremsstrahlung levels. We consider here the resulting fast-ion distribution function at selected times close to the end of each NBI heating phase, as illustrated in figure 1.

Figure 3 shows examples of the relevant kinetic profiles during one- and two-beam NBI heating phases, along with their uncertainties from IDA or CXRS. Also outlined are estimates of the global uncertainty on each parameter, based on the typical relative uncertainties on the profiles at the relevant times. To allow for the associated uncertainties in the TRANSP predictions, we ran additional simulations based on scaling up the electron density profiles and scaling down the temperature profiles, and vice versa, by factors represented by these global uncertainties (see also [39] for a similar approach). The net result is to modify the plasma collisionality $\nu_{ii}^* \propto n_i/T_i^2$ and $\nu_{ei}^* \propto n_i/(T_i^{1/2}T_e^{3/2})$ for ion–ion and electron–ion collisions, respectively, which in turn affects the slowing down rate of beam ions and hence the velocity-space density of fast ions at any given time. With standard error propagation and assuming $n_e \approx n_i$, the adopted global uncertainties on the kinetic profiles imply statistical uncertainties on ν_{ii}^* and ν_{ei}^* of 21% and 34%, respectively. As shown below, these values do indeed bracket the resulting variation in fast-ion density predicted with TRANSP.

3. Comparison between measurements and simulations

In this section we present fast-ion results from each of the three diagnostics and compare them with numerical predictions from TRANSP/NUBEAM. To first illustrate

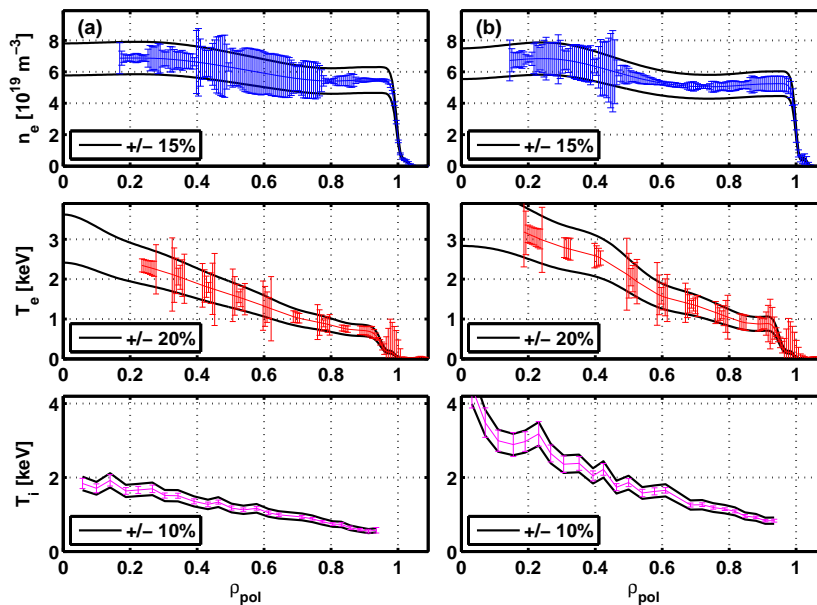


Figure 3. Example profiles of T_e and n_e from IDA and of T_i from CXRS and their uncertainties during (a) one-beam ($t = 4.04$ s) and (b) two-beam ($t = 5.45$ s) NBI heating phases in AUG discharge 29600. Black lines and their labels show the adopted representative uncertainties on each parameter. The CTS volume is located at $\rho_{\text{pol}} \simeq 0.36$.

the uncertainties on the theoretical predictions, figure 4 shows examples of the fast-ion distribution function $f(E, p, \mathbf{r})$ obtained with TRANSP in our high- and low-collisionality limits. Here E is the ion kinetic energy, and $p = v_{\parallel}/v$ the pitch (where v is the magnitude of the ion velocity and v_{\parallel} is that of the component anti-parallel to the local magnetic field). The distribution function is plotted for the location \mathbf{r} of the CTS volume, but the overall features are very similar for all FIDA volumes considered here. Note that the co-current (counter- \mathbf{B}) NBI geometry generates clearly visible velocity-space peaks at positive p , with $p < 0$ regions subsequently populated by pitch angle scattering. As anticipated, modifying ν^* strongly affects the predicted velocity-space density of fast ions. Integrating over energy and pitch to obtain the fast-ion density $n_{\text{fi}} = \int \int f(E, p) dE dp$ in the CTS volume, we find that n_{fi} varies by 30% and 27% around the baseline value for heating with Q3 and Q3+Q8, respectively, when going from high to low collisionality. As expected, this is similar to the allowed variation in ν^* itself implied by our adopted uncertainties.

3.1. CTS

Measured CTS spectra for this discharge are shown in figure 5 and compared with the corresponding forward model and its uncertainties at the six times indicated in figure 1. The model uncertainties are determined by those on the fast-ion contribution obtained from the different TRANSP runs. The model includes known transmission

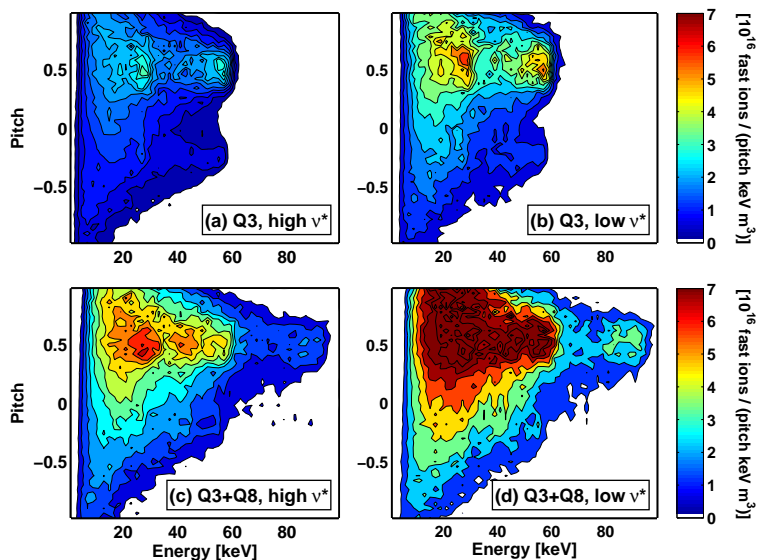


Figure 4. Predicted 2D fast-ion distribution functions $f(E, p)$ at the location of the CTS volume for (left column) high and (right column) low collisionality ν^* relative to our reference scenario. The top panel shows the case of heating with NBI Q3 only ($E = 60$ keV, $t = 4.04$ s), and the bottom panel that of NBI Q8 ($E = 93$ keV, $t = 5.54$ s) and Q3.

losses in the gyrotron line of the active-view CTS receiver [40], as well as a scaling factor of ~ 0.85 which accounts for any minor beam misalignment and sub-optimal receiver polarizer settings. This factor was derived from independent fits to our fast digitizer data of the bulk-ion spectra within $\lesssim 400$ MHz of the probe gyrotron frequency $f_{\text{gyr}} = 104.92$ GHz [31, 38]. In this frequency interval, the fast-ion contribution to the CTS spectra is entirely negligible.

It is important to emphasize that the model shown in figure 5 represents a forward model, i.e. a prediction of the experimental data (based on raytracing and on measurements from other diagnostics), rather than an actual fit to the fast-ion CTS data. Despite this, the comparison suggests good overall agreement within the uncertainties on measured and synthetic data. This is true also at large frequency shifts $|f - f_{\text{gyr}}| \gtrsim 0.7$ GHz, for which the TRANSP predictions suggest that fast ions begin to clearly dominate the measured spectra. A slight tendency of the baseline forward model to exceed the measurements can be seen in particular at $t = 4.04$ s where the derived bulk-ion scaling factor is slightly higher than in the other cases, but otherwise the data do not deviate significantly from the baseline model given the experimental uncertainties. The good agreement persists even for the final snapshot at $t = 5.84$ s where the experimental data are more noisy due to the NTM activity (cf. figure 1). This activity causes rapid fluctuations in the background level on timescales below our 6–8 ms time resolution, thus hampering accurate background subtraction and boosting the uncertainties in some frequency channels; nevertheless, the overall measured spectrum remains consistent with the synthetic one.

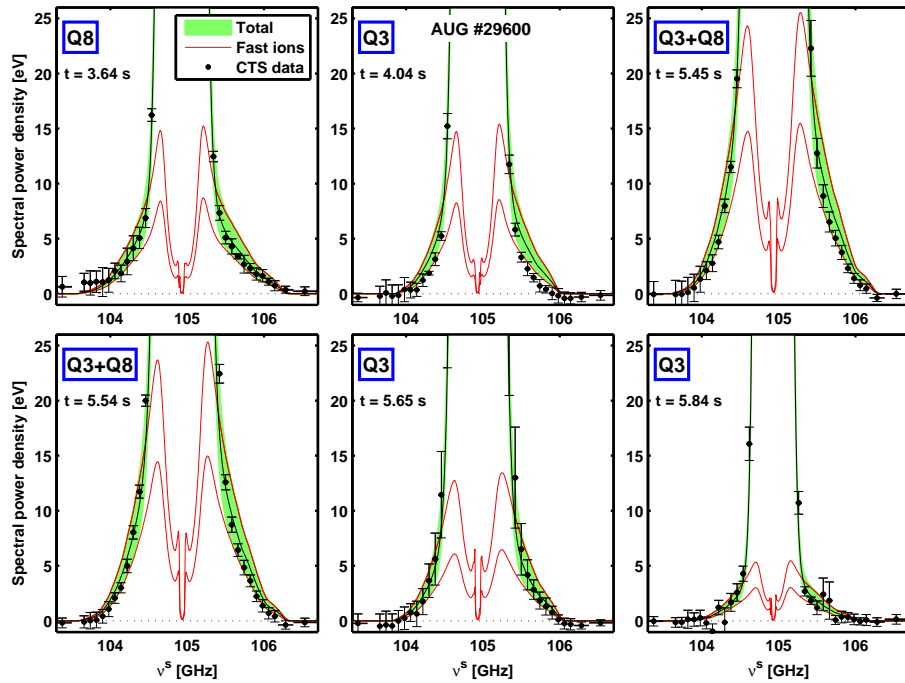


Figure 5. Measured CTS spectra (data points) compared to synthetic spectra based on TRANSP predictions. The baseline total TRANSP prediction is shown as a black line, and the associated uncertainties are shown as filled green regions. Red lines illustrate the uncertainties pertaining to the fast-ion contribution alone. These uncertainties represent the range resulting from TRANSP runs with different plasma collisionalities (see section 2). Uncertainties on measured data represent the standard deviation at a given frequency within a 50 ms time interval. Labels specify the active neutral beam injectors.

Other features evident in figure 5 include a small asymmetry about the probing frequency displayed by both computed and measured spectra. This is expected [41], given the adopted projection angle of $\phi = 106^\circ$ and the asymmetry in the beam ion distribution function (figure 4). Both measured and synthetic spectra are also seen to broaden in response to the different NBI injection energies and total heating power, and the slowing down of fast ions following the termination of two-beam NBI is evident in the bottom panel of figure 5. A reduced fast-ion signal at $t = 5.84$ s compared to at $t = 4.04$ s is also seen, as a consequence of the declining electron temperature and density toward the end of the discharge. Finally note that, thanks to the new dual-receiver approach, the residual CTS background is now fully consistent with being zero to sub-eV accuracy, as quantified by the signal level and receiver channel-to-channel scatter at large frequency shifts $\Delta f \geq 1.5$ GHz.

Fitting our CTS forward model to the experimental spectra yields 1D projections $g(u)$ of the fast-ion velocity distribution function. These are presented in figure 6 for projected ion velocities u beyond the Maxwellian bulk. Overall, the comparisons with the theoretical predictions demonstrate very good agreement during all NBI phases.

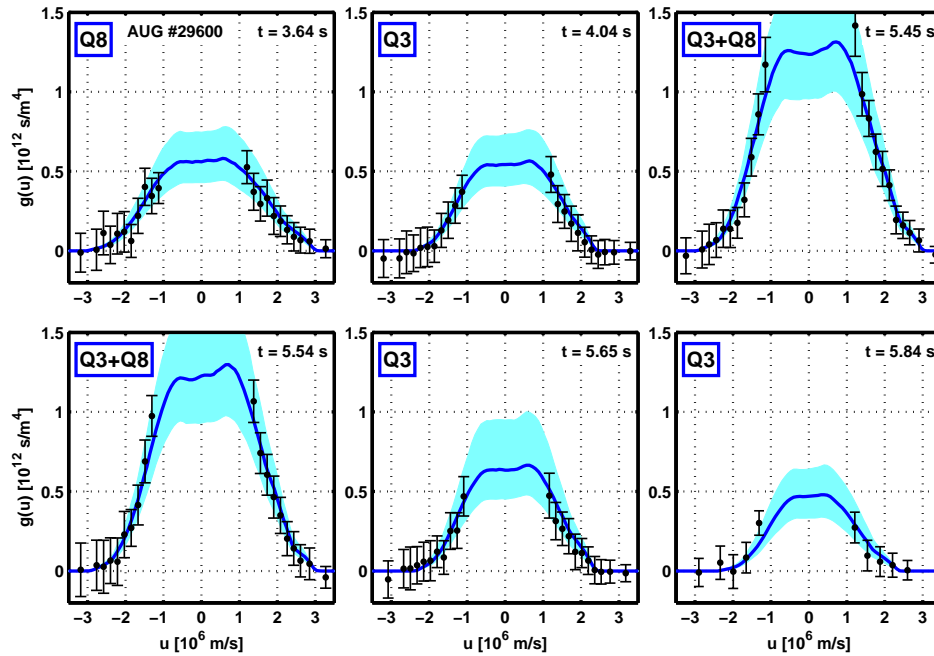


Figure 6. Fast-ion velocity distributions derived from CTS data integrated over 2 ms (data points), along with the baseline TRANSP prediction (blue line) and its uncertainties (filled). Times and labels correspond to those of figure 5.

Note that for $t = 5.84$ s, every other velocity node was omitted in the reconstruction of $g(u)$ in order to achieve a convergent fit from the somewhat noisier CTS spectrum. Again, a slight asymmetry about $u = 0$ in both the measured and predicted $g(u)$ is visible for the reason mentioned above, resulting in slightly higher $g(u)$ for positive u than for the corresponding negative u . As anticipated from figure 4, the uncertainties on the predicted $g(u)$ are found to be $\sim 30\%$.

Similarly to the case of the CTS spectra, the impact of increasing NBI heating energy can be discerned in 1D velocity space too. The experimentally inferred $g(u)$ shows clear evidence of increased (fast) ion content in the CTS volume during two-beam NBI, and the subsequent narrowing of the velocity distribution is also apparent. In figure 7 we compare the inferred velocity distributions during different NBI phases in more detail. Figure 7a shows $g(u)$ during one- and two-beam heating phases which both involve the more energetic ($E = 93$ keV) NBI Q8. A clear difference is seen, even though the velocity distributions here have comparable width. The broadening of the velocity distribution with increasing injection energy observed in figure 7b further demonstrates that we can clearly distinguish between single-beam heating with Q8 and the less energetic Q3 ($E = 60$ keV), again in good agreement with the numerical predictions.

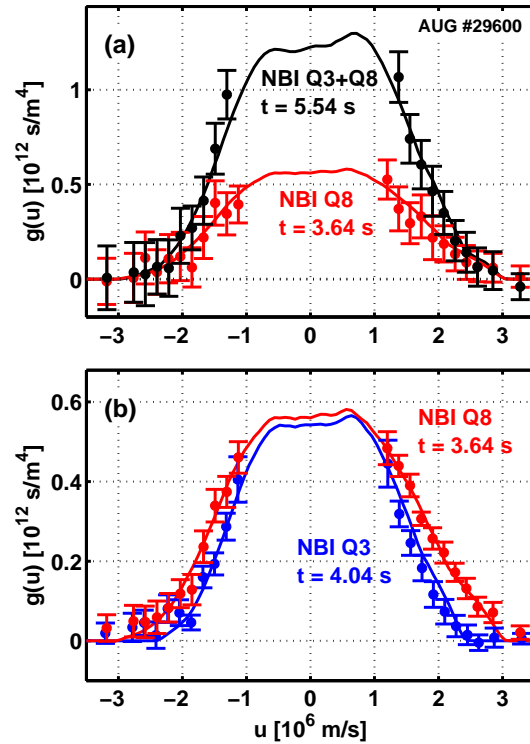


Figure 7. Comparison of velocity distributions inferred from CTS data during (a) one- and two-beam NBI heating, and (b) times corresponding to different single-beam heating energies. Lines represent the corresponding baseline TRANSP predictions. In (b), the fitted spectra have been averaged over 10 gyrotron pulses ($\Delta t = 80 \text{ ms}$) to improve the signal-to-noise ratio.

3.2. FIDA

The measured radial FIDA profiles are compared to the corresponding theoretical predictions in figure 8. The latter were obtained from synthetic FIDA spectra, generated by the FIDASIM code [42] on the basis of the fast-ion distribution function from our TRANSP simulations. The radial coordinate in the figure represents the locations of intersection between the FIDA lines of sight and the Q3 neutral beam, since the FIDA light is generated mainly along the path of this beam. The equivalent radial CTS positions, derived from mapping to equilibrium flux surfaces, range from $R = 1.82$ – 1.84 m . Given the D_α rest-frame wavelength of $\lambda_0 = 656.1 \text{ nm}$, the profiles show intensities integrated between wavelengths of 659.5 and 661.0 nm ; this provides a good signal-to-noise ratio for all injection energies given the mainly co-rotating fast ions generated by the neutral beams used in the discharge [5, 9]. The profiles have also been normalized by the observed neutral beam emission so as to provide a proxy for fast-ion densities. Plotted error bars include photon noise and CCD read-out noise, along with an assumed 10% error added in quadrature to account for uncertainties associated with background subtraction, intensity calibration, and beam emission normalization.

The comparison suggests reasonable agreement, especially in the plasma core, but

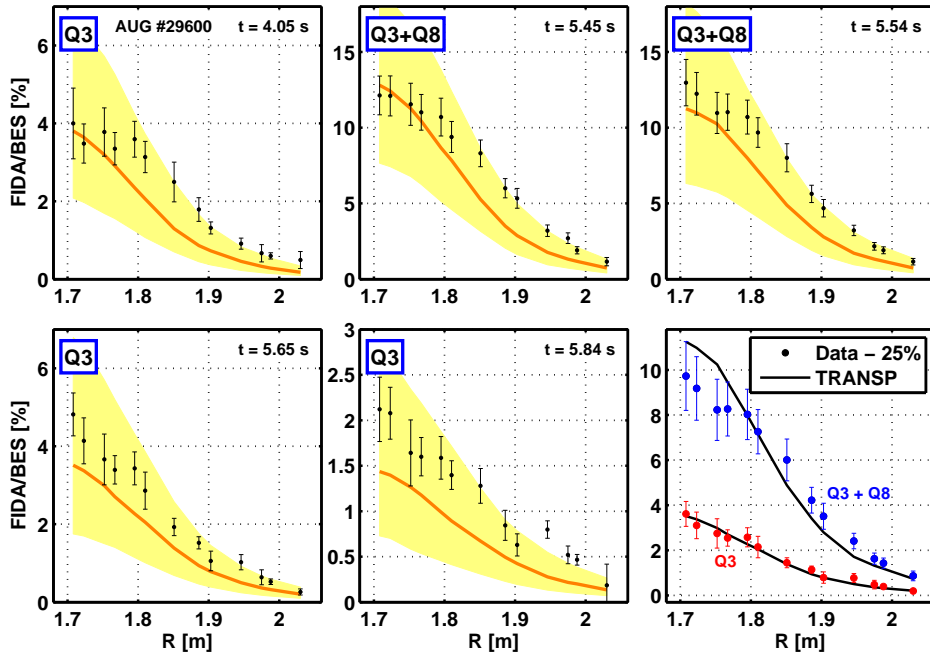


Figure 8. Comparison of FIDA results (data and error bars) to the baseline FIDASIM/TRANSP predictions (line) and their associated uncertainties (filled). Data points represent the 659.5–661.0 nm FIDA intensity, averaged over an 8 ms time interval and normalized by the measured beam emission (BES). Note the different ordinate axes. Labels are as in figure 5. The last panel compares the baseline TRANSP predictions during heating with NBI Q3 + Q8 ($t = 5.54$ s) and Q3 only ($t = 5.65$ s) to the measured data scaled down by 25%.

the baseline TRANSP prediction generally tends to lie below the observed signal outside the core. Scaling down the measured FIDA profiles by $\sim 25\%$ gives a better match to the baseline predictions, as shown in the final panel in figure 8. Nevertheless, FIDA measurements and theory still agree well within the TRANSP uncertainties. The only clear exception is at $t \approx 5.84$ s, where the observed signal at large radii significantly exceeds the predictions, plausibly due to the mode activity taking place at this time. As for CTS data, the increased fast-ion content in the measurement volume during two-beam NBI compared to one-beam NBI is evident, as is the subsequent slowing down of the fast ions, along with the reduced fast-ion signal at $t = 5.84$ s compared to at $t = 4.05$ s. Also note that the calculated theoretical uncertainties around the baseline prediction, of order 50% during two-beam heating, are somewhat larger than the corresponding value of $\sim 30\%$ found for the predicted fast-ion velocity-space density derived from CTS (figure 6). The reason is that the FIDASIM forward model, like the TRANSP simulation, depends on n_e and T_e and so is sensitive to the adopted variation in the kinetic profiles.

3.3. Neutron rates

Figure 9 displays the neutron rates predicted with TRANSP in comparison to the experimental values measured by the neutron rate detectors. The predicted neutron production is heavily dominated by fusion reactions between neutral beam particles and the target plasma (figure 9a). This is also highlighted by the clear dependence of the predicted and observed neutron rate on injected NBI energy, including the negligible neutron rate when no NBI is on (figure 9b). The TRANSP uncertainties range from 19 to 28%, in broad agreement with the adopted uncertainty on ν^* . Figure 9d shows that, while the neutron rate detectors are sensitive to neutrons from the full plasma volume, $\sim 70\%$ of the predicted neutron production takes place within $\rho_{\text{pol}} = 0.5$ (corresponding to within about 30 cm of the magnetic axis).

Again, we find good overall agreement between measurements and theory within the experimental and theoretical uncertainties. However, there is an indication of the measured rates slightly but systematically exceeding the baseline prediction, thus resembling the results from FIDA, specifically by an average of 12% during two-beam heating. Other discrepancies include a highly prominent spike in the observed neutron rate at $t \simeq 3.55$ s. However, the neutron rate signal is known to occasionally exhibit erroneous spikes [19]. Indeed, inspection of the raw signal from each of the five detectors suggests that the peak may not be real, as it is only clearly visible in the lowest-sensitivity detector (the ^{238}U fission chamber). Nevertheless, we note that the peak coincides with the onset of a 200 ms period of sawtooth activity as indicated by soft X-ray data.

Strong fluctuations in the neutron rates are also observed from the onset of the tearing mode at $t = 5.73$ s. These coincide roughly but not exactly with the occurrence of this mode, and they extend across the NBI turn-off. The fluctuations are associated with periodic spikes appearing at 10 ms intervals (i.e., at a frequency of 100 Hz) in the raw signal of all five neutron rate detectors, and in fact most prominently so in the least sensitive of them. This strongly suggests that this signal does not arise from neutrons in the plasma but might instead be related to some form of magnetic pickup. Support for this comes from the fact that no similar periodic variation is seen in any other diagnostic considered, nor does the observed 10 ms period match the 8 ms duty cycle of the CTS probe gyrotron in this part of the discharge. The fluctuations prevent us from clearly observing the slowing down of the fast ions at later times in the neutron rates, as otherwise seen in the numerical predictions and in the CTS and FIDA data.

4. Discussion

The measured results from all three diagnostics generally show good agreement with the TRANSP predictions within the combined experimental and theoretical uncertainties. The theoretical uncertainties, deriving from those on the measured kinetic profiles, are substantial however, and in general all diagnostic results formally agree with simulation predictions within those errors alone. The good agreement between measurement

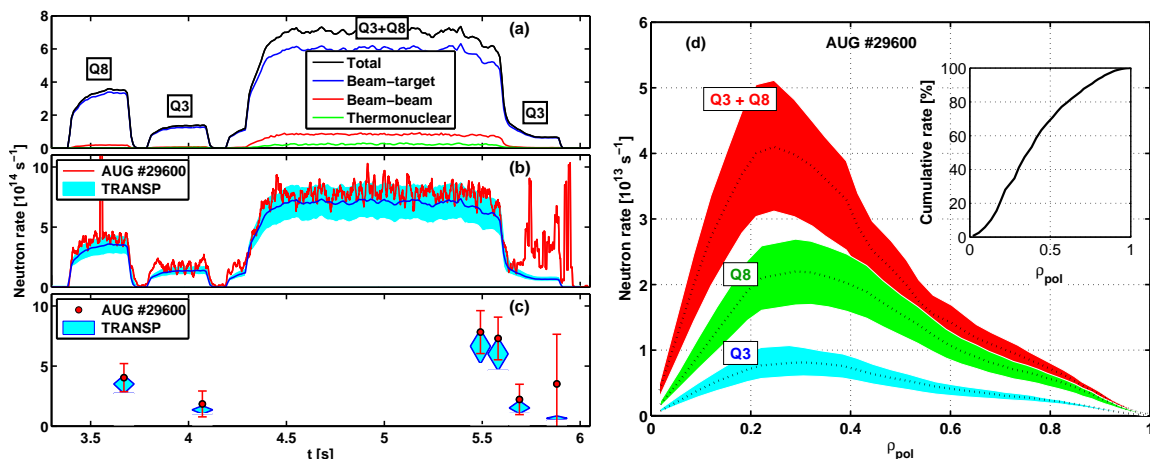


Figure 9. (a) The predicted contributions to the neutron rates from the different kinematic components, with NBI heating phases labelled. (b) Comparison of measured and predicted total neutron rates. The blue line and filled region represent the TRANSP prediction and its uncertainties. (c) Measured (mean and standard deviation over a 50 ms timescale) and predicted rates at the six fast-ion output times discussed above. (d) Predicted neutron rate profiles during the different heating phases. Dotted lines and filled regions show the baseline TRANSP predictions and their associated uncertainties. Inset shows the cumulative neutron rate within a given radius, normalized to the total value within $\rho_{\text{pol}} = 1$.

and theory for *all* three diagnostics suggests that systematic measurement errors are generally under control, and that the overall fast-ion physics in this discharge is reasonably well captured by our TRANSP simulations which assume neo-classical transport only. Notably, the anticipated slowing down of fast ions following the termination of two-beam NBI is evident in both CTS and FIDA data in agreement with the TRANSP predictions. The neutron rates in the final phases of the discharge fluctuate too strongly to reveal a similar effect, possibly due to the presence of an NTM.

Despite the overall consistency of synthetic and real data, some discrepancies emerge when comparing the measurements in more detail to our baseline TRANSP run. Fast-ion densities and fast-ion induced signals predicted by TRANSP are generally slightly lower than observed in the FIDA and neutron rate data, especially during two-beam NBI phases. This is particularly obvious for the FIDA measurements, which tend to exceed the baseline prediction at the 1σ measurement uncertainties. While examples of good agreement between FIDA measurements and TRANSP predictions exist at both AUG [9–11] and DIII-D [29], there are also some AUG discharges for which the simulated FIDA profile lies $\sim 30\%$ below measurements [5] as seen here. This has been ascribed to uncertainties in the FIDA intensity calibration and in the atomic transition rates and charge exchange cross sections implemented in the FIDASIM code. Other possibilities include a contribution from passive FIDA radiation not accounted for in measured data. However, this seems unlikely for the present discharge, for which only a small $\sim 5\%$ offset to the derived profiles is expected (section 2.2). Figure 8 suggests

that a larger offset of order 25% (i.e., similar to that found in [5]) is required to better match the data with the baseline TRANSP prediction.

For the measured neutron rates, good overall agreement to within $\sim 10\%$ is seen between experiment and the baseline TRANSP prediction. However, as for FIDA, the data show a systematic, albeit much less significant, tendency to exceed this prediction. As also suggested elsewhere [11], uncertainties in the measured Z_{eff} used in TRANSP could contribute to this slight mismatch [43], since these uncertainties translate into uncertainties in the deuterium density and hence in the dominant beam–target fusion rate. The more obvious discrepancies between theory and measurements, i.e. the presence of prominent spikes in the data (figure 9b), can be accounted for by the presence of erroneous spikes in the raw signal not arising from neutrons in the plasma.

For CTS, the good match found here between measurements and the associated 1D fast-ion velocity distribution $g(u)$ predicted by TRANSP represents the first example of quantitative agreement between theory and experiment at AUG during phases with both one- and two-beam NBI. It demonstrates that with the implementation of the dual-receiver technique, CTS at AUG has matured to a point where we can clearly identify the signature of different NBI power and injection energy on the measured properties of the fast-ion distribution in close agreement with theoretical expectations. Yet, subtle differences remain with respect to the TRANSP results, in which the experimental $g(u)$ in some cases slightly exceeds the baseline prediction at the velocities closest to the thermal bulk, while occasionally lying slightly below it at larger $|u|$. However, these discrepancies are, at most, marginally significant given the experimental uncertainties.

To facilitate the discussion of these various discrepancies with respect to TRANSP, we first note that the measurement volumes in both real space and velocity space are different among the diagnostics. In real space, CTS and FIDA data both represent localized measurements associated with small volumes, whereas the presented neutron rates are measured from the full plasma volume and so are not spatially resolved – although most neutrons are generated in the plasma core (figure 9). In fast-ion velocity space, it is instructive to assess the sensitivity of each diagnostic to different regions by means of weight functions $w(\phi, \epsilon, \Delta\epsilon, E, p, \mathbf{r})$ [29, 41, 44, 45]. These relate a fast-ion measurement $s(\phi, \epsilon, \Delta\epsilon)$, obtained for a given projection angle ϕ and spectral measurement range $\Delta\epsilon$ around a central value ϵ , to the fast-ion distribution function f ,

$$s(\phi, \epsilon, \Delta\epsilon) = \int \int \int w(\phi, \epsilon, \Delta\epsilon, E, p, \mathbf{r}) f(E, p, \mathbf{r}) dE dp d\mathbf{r}. \quad (3)$$

In the present case, $s(\phi, \epsilon, \Delta\epsilon)$ is represented either by $g(u)$ for CTS integrated over a projected velocity interval $\Delta\epsilon = \Delta u$, by the FIDA intensity $I(\lambda)$ integrated over a wavelength interval $\Delta\lambda$, or by the measured neutron rates $N(E_n)$ integrated over all supra-thermal neutron energies E_n . Example weight functions are illustrated in the left column of figure 10, highlighting the fast-ion velocity-space regions that can be accessed by each diagnostic for the viewing geometries chosen in this discharge. In the center and right columns of figure 10 we further show the product of the weight functions with the baseline TRANSP fast-ion distribution function f in the associated measurement

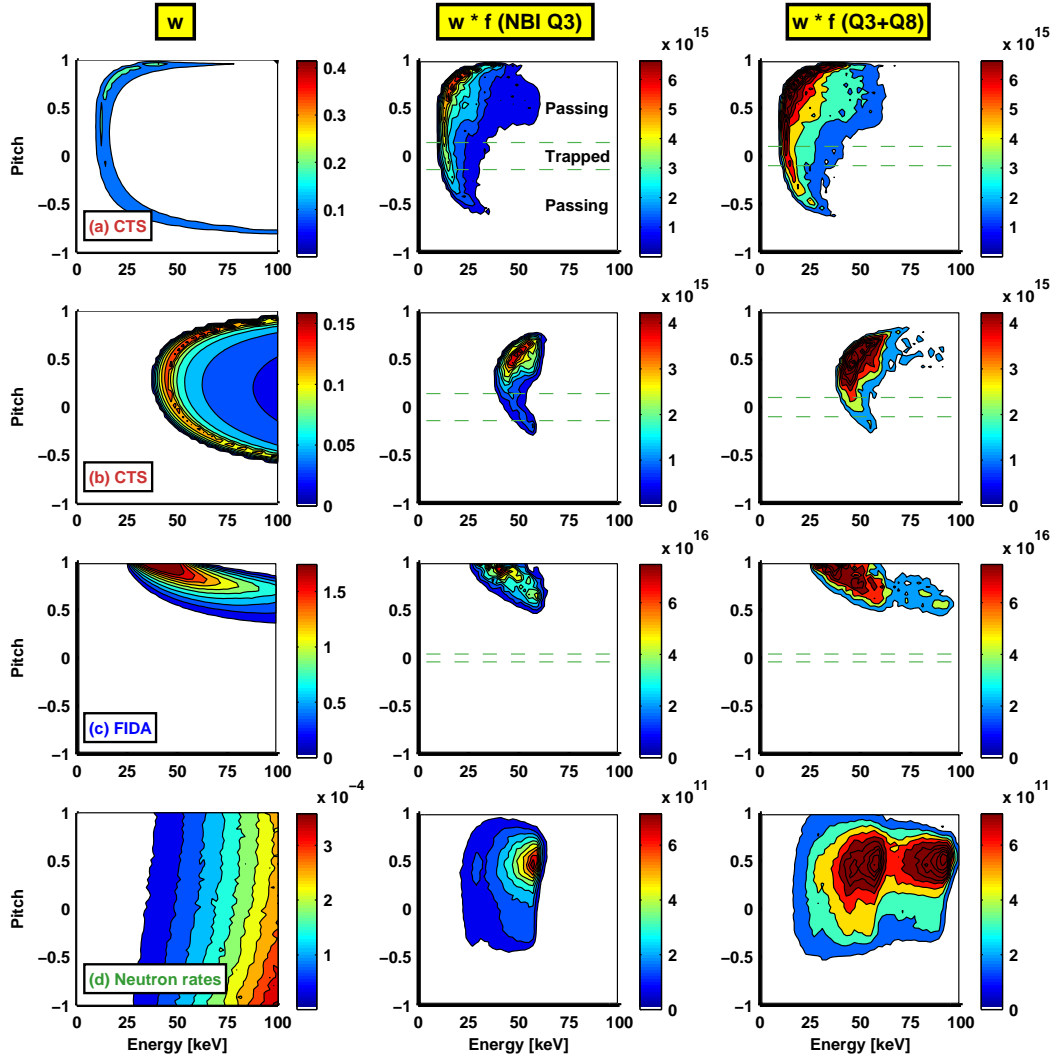


Figure 10. Weight functions $w(\phi, \epsilon, \Delta\epsilon, E, p, \mathbf{r})$ (left column) and their product with the fast-ion distribution function $f(E, p, \mathbf{r})$ from TRANSP during heating with NBI Q3 ($t = 4.04$ s, center column) and Q3+Q8 ($t = 5.45$ s, right column) in AUG discharge 29600. The two top panels show results for fast ions measured by CTS ($\phi = 106^\circ$), with velocities projected along \mathbf{k}^δ of (a) $u = +1 \times 10^6$ and (b) $u = +2 \times 10^6$ m/s (integrated over $\Delta u = 0.2 \times 10^6$ m/s). (c) FIDA results ($\phi = 12^\circ$) applying to a central FIDA channel ($R = 1.723$ m) integrated over $\Delta\lambda = 659.5\text{--}661.0$ nm. (d) Neutron rate weight function, approximated as a mean over all $\phi \in [0^\circ, 180^\circ]$ and integrated over all supra-thermal neutron energies, assuming the measured ion temperature and toroidal rotation velocity during Q3+Q8 heating ($t = 5.45$ s). Dashed horizontal lines in (a)–(c) mark the passing/trapped particle boundaries in the measurement volume as labeled.

volume at position \mathbf{r} . This illustrates the velocity-space regions that dominate the signal measured by each diagnostic during one- and two-beam NBI.

Given the width $\Delta f = 80$ MHz of a single CTS receiver channel, the weight functions shown for CTS have been integrated over $\Delta u = 0.2 \times 10^6$ m/s to match the corresponding resolution $\Delta u = 2\pi\Delta f/|\mathbf{k}^\delta|$ in projected velocity. For the scattering

geometry used in this discharge, CTS is seen to be sensitive to fast ions with a broad range in pitch, with a slight skewness toward positive pitch for positive projected velocities u . Hence, CTS in this configuration can access velocity-space regions associated with both passing ($|p| \gg 0$) and trapped ($|p| \sim 0$) fast ions. In contrast, the toroidal FIDA line-of-sight detects ions with a much narrower range in pitch, being mainly sensitive to co-current passing fast ions for the redshifted D_α wavelength range considered here and in figure 8. For the neutron rate detectors, weight functions were calculated with the formalism in [45] for beam-target reactions only, since these clearly dominate the predicted neutron production, cf. figure 9. Given the unrestricted field of view and the lack of a dependence of the detector sensitivity on the initial neutron energies, the accessible velocity-space region here extends across the entire relevant (E, p) space. Similarly to CTS, the neutron detectors are thus sensitive to both trapped and passing ions. However, the weights here increase rapidly with energy because of the strong energy dependence of the D-D fusion cross section. The asymmetry in pitch can be ascribed to plasma rotation; as the thermal ions are co-rotating, a counter-going fast ion has a higher velocity relative to the thermal ions, leading to a larger fusion cross section.

An immediate conclusion from figure 10 is that the signal measured by the various diagnostics in their adopted configuration arises in distinct but partly overlapping regions in fast-ion velocity space. Hence, fast ions probed by a given diagnostic and configuration include a sub-population that also contributes to the signal seen in the other data sets. In more detail, the FIDA signal, which is generally seen to exceed the baseline TRANSP prediction in this discharge, is dominated by the contribution from clearly passing fast ions and contains no footprint of trapped ions (this is true for all the 13 FIDA lines of sight considered here, as the trapped/passing boundary remains at $|p| \lesssim 0.4$ in all cases; nevertheless, we should note that for the specific times and FIDA channel represented in figure 10, there *is* actually good agreement between measurements and theory). The measured neutron rates, which show a smaller excess with respect to TRANSP, also have a contribution from clearly passing ions, but in this case trapped ions do contribute to the signal. Finally, CTS measurements, which generally agree well with TRANSP, also contain an imprint of trapped ions, albeit a sub-dominant one at the relevant projected velocities.

Taken together, the results are thus consistent with a picture in which measurements sensitive exclusively to passing fast ions tend to exceed the expectation from our baseline TRANSP simulation, while better agreement is seen for measurements more sensitive to deeply trapped fast ions. Since our theoretical predictions assume neo-classical fast-ion transport, this may point to the presence of anomalous diffusion generating slightly more passing fast ions in the measurement volumes than predicted by TRANSP. For example, in MHD quiescent AUG discharges with on-axis NBI (i.e. similar to AUG #29600), anomalous fast-ion diffusion has been shown to lower the toroidal-view FIDA signal in the plasma core and raise it at intermediate radii [11]. There is suggestive evidence of this in figure 8 when comparing the measurements to our TRANSP runs.

In the absence of strong MHD activity, as suggested by figure 1, a possible source for such anomalous diffusion could be micro-turbulence [46,47], although the importance of this for fast-ion redistribution has been questioned [48] and we have no measurements to directly test this scenario.

Another possibility is related to sawtooth-induced redistribution of fast ions into the measurement volumes [5, 49] and/or into more passing orbits [10]. As mentioned in section 2, soft X-ray data do indicate the presence of modest sawtooth activity from $t = 3.5\text{--}4.2$ s, with weak activity persisting until $t \approx 5.6$ s. In line with the indications from figures 6 and 8, this could be particularly relevant for the FIDA results, since these – unlike those of CTS – are associated solely with passing fast ions, and those ions tend to experience stronger redistribution by sawteeth than do trapped particles [6, 7, 10, 11]. The sawtooth inversion radius at $\rho_{\text{pol}} \approx 0.3$, as estimated from soft X-rays, roughly separates the innermost FIDA sight lines at $R \lesssim 1.80$ m from those further out. Hence, sawtooth activity might help explain the enhanced FIDA signal at intermediate radii at $t \lesssim 5.6$ s, but it remains unclear whether it can boost the FIDA signal at these radii *throughout* by the $\sim 25\%$ suggested by figure 8. For the CTS volume, the location at $\rho_{\text{pol}} \approx 0.36$ is comparable to that of the inversion radius, suggesting limited impact on the CTS measurements, as indeed supported by our results.

For completeness, we note that the neutron production at AUG is dominated by beam–target reactions and is not exclusively localized to the plasma core. Indeed, the total neutron rate predicted with TRANSP for the present discharge still displays a significant tail extending beyond $\rho_{\text{pol}} \approx 0.5$ (figure 9). Any sawteeth-induced fast-ion redistribution should thus, at most, mildly lower the measured neutron rates (and hence not aggravate the discrepancy with respect to TRANSP), unless fast ions were ejected from the plasma altogether. The latter possibility can probably be dismissed, on account of the mildly elevated neutron rates relative to the predictions.

5. Summary and outlook

We have presented the first, detailed comparison between numerical simulations using TRANSP/NUBEAM and measurements from CTS, FIDA, and neutron detectors, representing examples of the core fast-ion diagnostics at ASDEX Upgrade. We have also studied the sensitivity of the theoretical predictions to uncertainties in the input kinetic profiles, finding that predicted fast-ion densities can change by up to 30% when scaling these input profiles within their estimated limits. Taking these uncertainties on the theoretical predictions into account, we find that measurements from all three diagnostics are generally consistent with the TRANSP predictions during phases with either one and two neutral beam injection sources. For CTS, this represents the first demonstration of a convincing quantitative match between theory and fast-ion results at AUG during different NBI phases.

The observation that measurements from three core fast-ion diagnostics are *simultaneously* consistent with the associated TRANSP predictions strongly suggests

that the fast ions in this discharge slow down according to neo-classical theory. Moreover, it points to a significant degree of internal consistency among the diagnostics, which is made more convincing still by the observation that these diagnostics probe partially overlapping regions in fast-ion velocity space. Our results hence bode well for attempts to combine CTS, FIDA, and neutron rates in a multi-diagnostic velocity-space reconstruction of the 2D fast-ion distribution function at AUG. The non-localized measurement volume for neutron rates renders reconstruction involving these somewhat more complex, but still tractable, with the spatially concentrated neutron production limiting the relevant volume considerably. With the work in [26–28, 45, 50], the analytical framework for such multi-diagnostic reconstructions is in principle in place. Encouragingly, our results provide the first experimental support for the feasibility of such reconstructions.

Acknowledgements

We gratefully acknowledge useful discussions with R Neu. This project has received funding from the European Union’s Horizon 2020 research and innovation programme under grant agreement number 633053. The views and opinions expressed herein do not necessarily reflect those of the European Commission.

References

- [1] Campbell D J *et al* 1988 Stabilization of Sawteeth with Additional Heating in the JET Tokamak *Phys. Rev. Lett.* **60**, 2148–51
- [2] Heidbrink W W and Sadler G J 1994 The behaviour of fast ions in tokamak plasmas *Nucl. Fusion* **34** 535–615
- [3] Pinches S D *et al* 2004 The role of energetic particles in fusion plasmas *Plasma Phys. Control. Fusion* **46(12B)** B187–B200
- [4] García-Muñoz M *et al* and The ASDEX Upgrade Team 2010 Fast-ion losses induced by ACs and TAEs in the ASDEX Upgrade tokamak *Nucl. Fusion* **50** 084004
- [5] Geiger B, García-Muñoz M, Heidbrink W W, McDermott R M, Tardini G, Dux R, Fischer R, Igochine V and the ASDEX Upgrade Team 2011 Fast-ion D-alpha measurements at ASDEX Upgrade *Plasma Phys. Control. Fusion* **53** 065010
- [6] Nielsen S K *et al* 2011 Dynamics of fast ions during sawtooth oscillations in the TEXTOR tokamak measured by collective Thomson scattering *Nucl. Fusion* **51** 063014
- [7] Muscatello C M, Heidbrink W W, Kolesnichenko Ya I, Lutsenko V V, Van Zeeland M A and Yakovenko Yu V 2012 Velocity-space studies of fast-ion transport at a sawtooth crash in neutral-beam heated plasmas *Plasma Phys. Control. Fusion* **54** 025006
- [8] Lauber Ph, Classen I G J, Curran D, Igochine V, Geiger B, da Graça S, García-Muñoz M, Maraschek M, McCarthy P and the ASDEX Upgrade Team 2012 NBI-driven Alfvénic modes at ASDEX Upgrade *Nucl. Fusion* **52** 094007
- [9] Geiger B, Dux R, McDermott R M, Potzel S, Reich M, Ryter F, Weiland M, Wunderlich D, ASDEX Upgrade Team and García-Muñoz M 2013 Multi-view fast-ion D-alpha spectroscopy diagnostic at ASDEX Upgrade *Rev. Sci. Instrum.* **84** 113502
- [10] Geiger B *et al* 2014 Fast-ion transport in the presence of magnetic reconnection induced by sawtooth oscillations in ASDEX Upgrade *Nucl. Fusion* **54** 022005

- [11] Geiger B *et al* 2015 Quantification of the impact of large and small-scale instabilities on the fast-ion confinement in ASDEX Upgrade *Plasma Phys. Control. Fusion* **57** 014018
- [12] Meo F *et al* 2008 Commissioning activities and first results from the collective Thomson scattering diagnostic on ASDEX Upgrade (invited) *Rev. Sci. Instrum.* **79**(10) 10E501
- [13] Meo F *et al* 2010 First results and analysis of collective Thomson scattering (CTS) fast ion distribution measurements on ASDEX Upgrade *J. Phys.: Conf. Ser* **227** 012010
- [14] Salewski M *et al* 2010 Comparison of fast ion collective Thomson scattering measurements at ASDEX Upgrade with numerical simulations *Nucl. Fusion* **50** 035012
- [15] Furtula V, Salewski M, Leipold F, Michelsen P K, Korsholm S B, Meo F, Moseev D, Nielsen S K, Stejner M and Johansen T 2012 Design and performance of the collective Thomson scattering receiver at ASDEX Upgrade *Rev. Sci. Instrum.* **83** 013507
- [16] Nielsen S K *et al* and The ASDEX Upgrade Team 2015 Measurements of the fast-ion distribution function at ASDEX Upgrade by collective Thomson scattering using active and passive views *Plasma Phys. Control. Fusion* **57** 035009
- [17] García-Muñoz M, Fahrbach H-U, Zohm H and the ASDEX Upgrade Team 2009 Scintillator based detector for fast-ion losses induced by magnetohydrodynamic instabilities in the ASDEX upgrade tokamak *Rev. Sci. Instrum.* **80** 053503
- [18] Kurki-Suonio T, Hynönen V, Suttrop W, Fahrbach H-U, Stober J and the ASDEX Upgrade Team 2006 Edge Fast Ion Distribution –Benchmarking ASCOT against Experimental NPA Data on ASDEX Upgrade *Europhys. Conf. Abstracts* **30I** P2.145
- [19] Zohm H, Bosch H-S, Gruber O, Neu R, Schweiss H-P, Stäbler A, Stober J and the ASDEX Upgrade Team 2002 Neutron Production in High Performance Scenarios in ASDEX Upgrade *Europhys. Conf. Abstracts* **26B** P1.043
- [20] Höhbauer C 2010 Modellierung der Neutronenproduktion in Plasmaentladungen am Fusionsexperiment ASDEX Upgrade *IPP Report* 1/339, Max-Planck-Institut für Plasmaphysik
- [21] Giacomelli L, Zimbal A, Tittelmeier K, Schuhmacher H, Tardini G, Neu R and the ASDEX Upgrade Team 2011 The compact neutron spectrometer at ASDEX Upgrade *Rev. Sci. Instrum.* **82** 123504
- [22] Tardini G, Zimbal A, Esposito B, Gagnon-Moisan F, Marocco D, Neu R, Schuhmacher H and the ASDEX Upgrade Team 2012 First neutron spectrometry measurements in the ASDEX Upgrade tokamak *JINST* **9** C03004
- [23] Nocente M *et al* and The ASDEX Upgrade Team 2012 Gamma-ray spectroscopy measurements of confined fast ions on ASDEX Upgrade *Nucl. Fusion* **52** 094021
- [24] Stroth U *et al* 2013 Overview of ASDEX Upgrade results *Nucl. Fusion* **53** 104003
- [25] Salewski M *et al* and The ASDEX Upgrade team 2012 Tomography of fast-ion velocity-space distributions from synthetic CTS and FIDA measurements *Nucl. Fusion* **52** 103008
- [26] Salewski M *et al* 2013 Combination of fast-ion diagnostics in velocity-space tomographies *Nucl. Fusion* **53** 063019
- [27] Jacobsen A S *et al* and the ASDEX Upgrade Team 2013 How to compute velocity-space tomographies using several fast-ion diagnostics *Europhys. Conf. Abstracts* **37D** O6.512
- [28] Salewski M *et al* 2014 Measurement of a 2D fast-ion velocity distribution function by tomographic inversion of fast-ion D-alpha spectra *Nucl. Fusion* **54** 023005
- [29] Heidbrink W W, Luo Y, Burrell K H, Harvey R W, Pinsker R I and Ruskov E 2007 Measurements of fast-ion acceleration at cyclotron harmonics using Balmer-alpha spectroscopy *Plasma Phys. Control. Fusion* **49** 1457-1475
- [30] Rasmussen J *et al* and The ASDEX Upgrade Team 2014 Improved Collective Thomson Scattering measurements of fast ions at ASDEX Upgrade *AIP Conf. Proc.* **1612** 117–20
- [31] Stejner M *et al* and The ASDEX Upgrade Team 2014 Resolving the bulk ion region of millimeter-wave collective Thomson scattering spectra at ASDEX Upgrade *Rev. Sci. Instrum.* **85** 093504
- [32] Bindslev H 1993 3-wave mixing and Thomson scattering in plasmas *Plasma Phys. Control. Fusion* **35** 1615–40

- [33] Bindslev H 1996 A quantitative study of scattering from electromagnetic fluctuations in plasmas *J. Atmos. Terr. Phys.* **58** 983–9
- [34] Pankin A, McCune D, Andre R, Bateman G and Kritz A 2004 The tokamak Monte Carlo fast ion module NUBEAM in the National Transport Code Collaboration library *Comp. Phys. Comm.* **159** 157–84
- [35] Bindslev H 1999 Methods for optimizing and assessing diagnostic capability, demonstrated for collective Thomson scattering (invited) *Rev. Sci. Instrum.* **70** 1093–9
- [36] Bindslev H and Hansen F R 1991 Numerical Investigations of the Propagation of Electromagnetic Millimetre Waves in a Fluctuating Plasma – Impact of Density Fluctuations on JET Alpha Particle Diagnostic, *JET Internal Report JET-IR(91)02*
- [37] Fischer R, Fuchs C J, Kurzan B and Wolfrum E 2010 Integrated Data Analysis of Profile Diagnostics at ASDEX Upgrade *Fusion Sci. Technol.* **58** 675–84
- [38] Stejner M *et al* and The ASDEX Upgrade Team 2015 Plasma rotation and ion temperature measurements by CTS at ASDEX Upgrade *Plasma Phys. Control. Fusion* **57** 062001
- [39] Luo Y, Heidbrink W W, Burrell K H, Ruskov E and Solomon W M 2007 Fast-ion D_α measurements and simulations in quiet plasmas *Phys. Plasmas* **14** 112503
- [40] Wagner D *et al* 2008 Status of the new multi-frequency ECRH system for ASDEX Upgrade *Nucl. Fusion* **48** 054006
- [41] Salewski M *et al* 2011 On velocity space interrogation regions of fast-ion collective Thomson scattering at ITER *Nucl. Fusion* **51** 083014
- [42] Heidbrink W W, Liu D, Luo Y, Ruskov E and Geiger B 2011 A Code that Simulates Fast-Ion D-alpha and Neutral Particle Measurements *Commun. Comp. Phys.* **10** 716–41
- [43] Tardini G, Höhbauer C, Fischer R, Neu R and the ASDEX Upgrade Team 2013 Simulation of the neutron rate in ASDEX Upgrade H-mode discharges *Nucl. Fusion* **53** 063027
- [44] Salewski M, Geiger B, Moseev D, Heidbrink W W, Jacobsen A S, Korsholm S B, Leipold F, Madsen J, Nielsen S K, Rasmussen J, Stejner M, Weiland M and the ASDEX Upgrade Team 2014 On velocity-space sensitivity of fast-ion D-alpha spectroscopy *Plasma Phys. Control. Fusion* **56** 105005
- [45] Jacobsen A S, Salewski M, Eriksson J, Ericsson G, Korsholm S B, Leipold F, Nielsen S K, Rasmussen J, Stejner M 2015 Velocity-space sensitivity of neutron spectrometry measurements *Nucl. Fusion* **55** 053013
- [46] Günter S *et al* 2007 Interaction of energetic particles with large and small scale instabilities *Nucl. Fusion* **47** 920
- [47] Heidbrink W W, Park J M, Murakami M, Petty C C, Holcomb C and Van Zeeland M A 2009 Evidence for Fast-Ion Transport by Microturbulence *Phys. Rev. Lett.* **103** 175001
- [48] Pace D *et al* 2013 Energetic ion transport by microturbulence is insignificant in tokamaks *Physics of Plasmas* **20** 056108
- [49] Nielsen S K *et al* 2010 Fast-ion redistribution due to sawtooth crash in the TEXTOR tokamak measured by collective Thomson scattering *Plasma Phys. Control. Fusion* **52** 092001
- [50] Jacobsen A S, Salewski M, Eriksson J, Ericsson G, Hjalmarsson A, Korsholm S B, Leipold F, Nielsen S K, Rasmussen J and Stejner Pedersen M 2014 Velocity-space sensitivity of the time-of-flight neutron spectrometer at JET *Rev. Sci. Instrum.* **85** 11E103